Computational model of fractal interface formation in bacterial biofilms

Caelan Brooks,[1,2,3,4,*] Meiyi Yao,[5,*] Jake T. McCool,[2,3,6] Alan Gillman,[6,†] Gürol M. Süel,[6] Andrew Mugler,[1] and Joseph W. Larkin[2,3,7,‡]

[1]*Department of Physical Sciences, Kutztown University of Pennsylvania, Kutztown, Pennsylvania, USA*
[2]*Department of Physics, Boston University, Boston, Massachusetts, USA*
[3]*Biological Design Center, Boston University, Boston, Massachusetts, USA*
[4]*Department of Physics, Harvard University, Cambridge, Massachusetts, USA*
[5]*Department of Physics and Astronomy, University of Pittsburgh, Pittsburgh, Pennsylvania, USA*
[6]*Division of Biological Sciences, University of California San Diego, La Jolla, California, USA*
[7]*Department of Biology, Boston University, Boston, Massachusetts, USA*

(Received 16 December 2024; accepted 9 September 2025; published 8 December 2025)

Bacteria benefit from cellular heterogeneity: cells differentiate into diverse gene expression states. As colonies grow, cellular phenotypes arrange into spatial patterns. To uncover the functional role of these emergent patterns, we must understand how they arise from cellular growth and mechanical interactions. Here we present a simple, agent-based model to predict patterns of motile and extracellular matrix-producing cells in biofilms of *Bacillus subtilis*. By incorporating phenotypic inheritance, mechanical interactions, and peripheral motile cell dispersal, our model predicts the emergence of a pattern: matrix cells surround a fractal-like interior motile population. We find that, while some properties of the motile-matrix interface depend on initial conditions, the motile distribution at large radii depends solely on the model's growth mechanism. The phenotypic interface exhibits a fractal dimension that increases as biofilms grow but reaches a maximum as the peripheral layer of matrix cells exceeds the capacity of the inner cells to push it out of the way. By varying parameters, we find correlations between the interface fractal dimension and expansion of motile cells. We validate findings using experiments on *B. subtilis* biofilms in microfluidics. Our model demonstrates the emergence of colony-level phenotypes from single cell-level interactions and cells modifying their own environment.

DOI: 10.1103/2zm9-r3qs

I. INTRODUCTION

In stressful environments, microbes differentiate into heterogeneous states of physiology and gene expression [1–3]. For example, *Bacillus subtilis* bacteria generate multiple cell types characterized by distinct gene expression states [4], including matrix producers, which synthesize extracellular polymers to bind cells together into biofilms [5] and motile cells, which exhibit swimming and swarming behavior [6]. As cells differentiate into these states, they change how they interact with each other and the environment [7,8]. Surface-adhered biofilm colonies contain cells in numerous phenotypic states [9,10], leading microbiologists to make analogies between the growth of biofilms and cell differentiation during the development of multicellular organisms [11–13].

Bacterial biofilms are characterized by the synthesis of an extracellular matrix, which attaches cells to surfaces and to each other [14]. In *B. subtilis*, matrix production, and consequently biofilm formation, is regulated by a master transcription factor that lifts repression on matrix production genes to form biofilms [15]. This gene regulatory switch is itself activated by a signaling cascade that takes in multiple streams of environmental information, including cell density and metabolic conditions [16,17]. As a consequence, *B. subtilis* often forms biofilms at high cell density, but many environments can trigger biofilm formation [18]. Despite matrix production being necessary for biofilm formation, many non-matrix-producing cells are found in *B. subtilis* biofilms, including motile cells [10,19] The origin of this phenotypic heterogeneity is still an area of active research, though it may arise from noise and multistability in gene regulatory circuits [20,21], and heterogeneity need not be present in initial cells for a biofilm to exhibit phenotypic heterogeneity [22]. The motile and matrix phenotypes in *B. subtilis* are regulated by a transcription factor network whose interactions cause the two phenotypes to be mutually exclusive [6,23] and heritable [21]. Within biofilms, these phenotypic states form repeatable spatiotemporal patterns [10,19]. We find that in microfluidic *B. subtilis* biofilms, motile and matrix-producing ("matrix" for short) cells form a pattern where matrix cells surround a fractal-like population of motile cells (Fig. 1). Despite the

[*]These authors contributed equally to this work.
[†]Present Address: Evident Scientific, Waltham, Massachusetts, USA.
[‡]Contact author: jwlarkin@bu.edu

Published by the American Physical Society under the terms of the Creative Commons Attribution 4.0 International license. Further distribution of this work must maintain attribution to the author(s) and the published article's title, journal citation, and DOI.

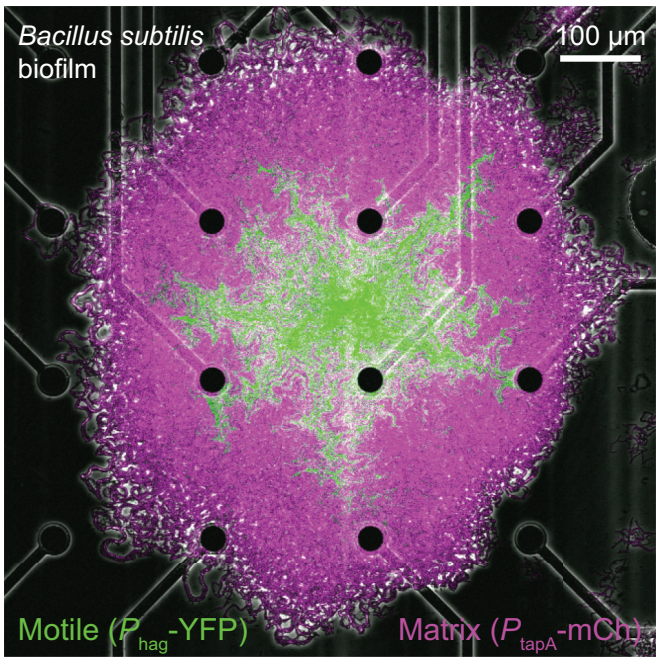


FIG. 1. Phenotypic Patterning in a *Bacillus subtilis* Biofilm. Fluorescence image of a *B. subtilis* biofilm grown in a microfluidic device. False color green is the signal from a reporter on motility genes (P_{hag}-YFP). Magenta is the signal from a matrix production reporter (P_{tapA}-mCherry).

robustness of these patterns, we do not understand how they arise. To eventually explore the functional role of spatiotemporal patterns in bacterial colonies, we must develop models that predict patterns based on biological and physical factors that may create them, such as phenotypic inheritance in dividing cells [1] and mechanical interactions among bacteria [24].

Agent-based models provide a framework to ask how colony-scale phenomena emerge from the properties of individual bacterial cells. Such simulations have been used to show how mechanical interactions lead to cellular reordering in dense colonies [25], how cell shape affects the spatial partitioning of different species within microbial communities [26], and how mechanical interactions and cell shape together lead to fractal patterning in bacterial layers [27]. Furthermore, agent-based simulations have been used to account for feedback of mechanical interactions on cell growth [28] and the interplay of mechanics with other forms of interaction like quorum sensing [29]. Nevertheless, the combined effects of mechanical interactions and heritable phenotypic differences in those interactions remain poorly understood.

Here, we present a simple, agent-based, computational model of growing populations of *B. subtilis* to ask how mechanical interactions among phenotypes can drive pattern formation. The model takes into account three key factors in the development of motile-matrix patterning. First, cell phenotypes are mutually exclusive and heritable: cells are either motile or matrix producing, with daughter cells perfectly inheriting their parent's phenotype. Second, motile cells exposed to the edge of the colony will "disperse" and swim away. Third, when a cell on the colony interior divides, it must shove other cells out of the way to make space for the new cell. Matrix cells resist shoving more strongly than motile cells.

From our model's three simple rules for cellular division, motion, and interactions, we can simulate biofilm growth from an initial inoculum of bacteria. The model produces a biofilm with an interior population of motile cells surrounded by matrix cells. The interface between these two populations is not circular, but rather develops a characteristic roughness pattern. Whereas concurrent work uses continuum modeling to investigate the emergence and dominant wavelengths of this pattern [30], we use our agent-based model to characterize its dynamics and self-similar, or fractal, properties. By varying our model parameters and extracting the fractal dimension of simulated biofilms, we find that our model predicts a correlation between the fractal dimension and the radial expansion of motile cells across a wide range of parameter values. We find that both the fractal dimension and the extent of radial expansion are consistent with our experimental data from *B. subtilis* biofilms grown in microfluidic devices [31]. Our model shows how population-level phenomena can emerge from the heterogeneous mechanical cellular interactions.

II. RESULTS

A. Emergence of motile-matrix patterns in experimental *B. subtilis* biofilms

Previous experiments have observed spatiotemporal successions of motile and matrix cells in three dimensional *B. subtilis* biofilms [10,19]. We wanted to observe the patterns of motile and matrix cells in conditions where cells did not have the freedom to grow into the z dimension so we grew *B. subtilis* biofilms in a microfluidic device confined to a thickness of one to three cell layers [31]. We used a strain with separate transcriptional fluorescent reporters for promoters of motility genes and matrix production genes [10]. Two key observations emerged from this experiment. First, upon initial cell loading, colonies did not exhibit distinguishable patterns of motile or matrix cells (we cannot rule out that there was an early pattern, but fluorescent reporter intensity was too low for us to detect it). Second, after approximately 16 h of growth, biofilms had organized into a distinctive pattern, with a fractal-like population of motile cells surrounded by matrix-producing cells (Fig. 1). From our observations, two questions arose: (1) How, if at all, does the initial arrangement of motile and matrix cells influence that pattern that arises during growth? (2) What mechanism leads to such a pattern? We sought to create a computational model that could account for these observations.

B. An agent-based, mechanistic cell growth model

We model the dynamics of biofilm growth using sites on a two-dimensional square lattice (Fig. 2). For computational simplicity, we restrict ourselves to parameters for which simulated phenotypic patterns develop when biofilms grow to thousands of sites, whereas experimental biofilms may typically grow to hundreds of thousands of cells. Therefore, each site can be thought of as a coarse-grained packet of cells of the same phenotype (motile or matrix). Furthermore, as described below, we assume no preferential direction for site growth

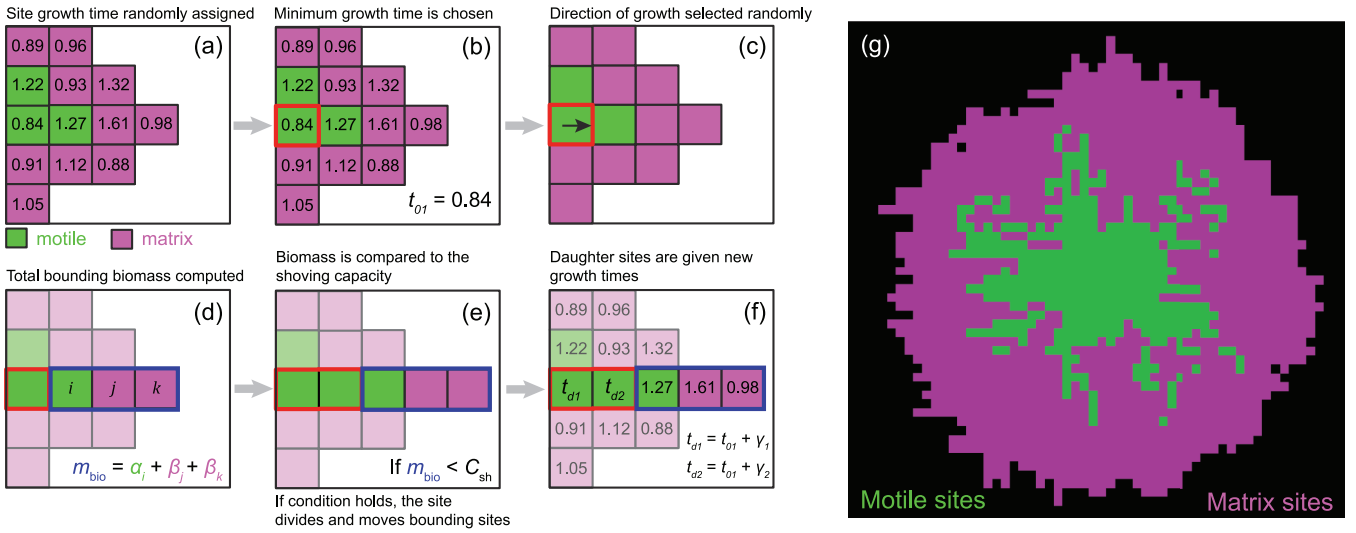


FIG. 2. Agent-based biofilm growth model. (a)–(f) Growth and displacement mechanism: (a) Growth times are drawn from a Gaussian distribution and are assigned to each site. (b) The lattice site with the minimum growth time (outlined in red here) is selected and given the opportunity to grow, where t_{01} is the initial growth time. (c) The direction of growth is chosen randomly from four options. (d) If the site is not on the edge, the total biomass (m_{bio}) will be measured in the growth direction. The biomass of each site type is represented by α and β, which are Gaussian distributed with different means ($\langle\beta\rangle > \langle\alpha\rangle$). (e) The biomass is pushed under the condition $m_{bio} < C_{sh}$. (f) New sites are given growth times based on t_{01}. (g) Resulting pattern once interior motile sites become frozen because biomass exceeds shoving capacity. Parameter values are $C_{sh} = 12$, $\langle\alpha\rangle = 1$, $\langle\beta\rangle = 2$, and $\sigma_\alpha = \sigma_\beta = 0.1$.

apart from steric hindrance due to existing sites (although we later checked for the effects of preferential growth direction). This assumption avoids lattice artifacts that can arise in agent-based models [32] and is consistent with sites being packets of cells, given that the packets are larger than the length scale over which cells align due to their rodlike shape [33]. We later accounted for cellular coarse-graining when comparing to the experimental data.

We initiate the system by creating an inoculum of sites containing both motile and matrix phenotypes. Each site is given a growth time that acts as an internal clock, indicating when it is time to divide [Fig. 2(a)]. These growth times are randomly drawn from a normal distribution centered at 1 (in units of the average division cycle time), with a standard deviation of 0.1 (the typical order of magnitude of variability in doubling time in *B. subtilis*) [21].

At each step of the simulation, the site with the minimum growth time is chosen [Fig. 2(b)]. The chosen site then goes through a process of determining if and how to divide and produce a daughter. If the site is on the edge of the biofilm, it chooses from the neighboring empty spaces with equal probability and grows into one of them, filling the space with a daughter. Daughter sites inherit their mother's phenotype with no switching. The two new sites are then assigned random growth times. If instead the dividing site is surrounded by others [Fig. 2(c)], then it must shove those sites out of the way to create space for a new daughter [Fig. 2(d)]. The direction of growth is chosen with an equal probability of being up, down, left, or right. We then compute the total biomass (m_{bio}) between the chosen site and the edge of the growing colony in the chosen direction [Fig. 2(d)]. Each site has a different biomass, with motile and matrix biomasses being drawn randomly from distributions with different means, but the same variance. Motile biomass is $\langle\alpha\rangle \pm \sigma_\alpha$ and matrix biomass is $\langle\beta\rangle \pm \sigma_\beta$, where $\langle\beta\rangle > \langle\alpha\rangle$ and $\sigma_\beta = \sigma_\alpha$. We call the parameter biomass, but it represents multiple physical properties that contribute to a site's resistance to physical pushing, such as surface adhesion. Experimental measurements of adhesion for matrix-producing and nonproducing cells that are directly comparable to our model parameters have not been made, but those that exist suggest our parameter values are not qualitatively incorrect [34]. Setting $\langle\beta\rangle > \langle\alpha\rangle$ is a key aspect of the model. Having matrix and motile sites contribute differently to mechanical interactions implements similar concepts to continuum models of phenotypic interfaces, which have shown that purely mechanical effects can drive pattern formation in bacterial communities [30]. We hypothesized that different mechanical interactions of motile and matrix sites in our agent-based model would drive the formation of distinct motile and matrix patterns. Because matrix sites have greater biomass in our model, they offer more resistance to pushing by growth. This choice reflects the fact that biofilm matrix cells produce polymers that adhere them to the substrate and to each other [35].

We further assume a constraint on how deep into the biofilm a site can grow and shove biomass. Previous agent-based models have assumed cells beyond a certain depth in a colony do not grow and push biomass due to fundamental constraints such as nutrient depletion [29]. We represent the constraint with a parameter called the shoving capacity, C_{sh}. If the bounding biomass is less than or equal to C_{sh}, then the stack of sites is pushed out of the way, and a new daughter site is created [Fig. 2(e)]. The original growing site and the new daughter then receive new growth times [Fig. 2(f)] and the simulation progresses by choosing the site with the next minimum growth time. If the $m_{bio} < C_{sh}$ condition is not met for the chosen direction, the site will not grow in any direction and instead be given a new growth time drawn from the

distribution. This site has the opportunity to grow in the future once it becomes the minimum growth time and if it can push in its new chosen direction, otherwise it will be given a new growth time again. Our model differs from previous agent-based models [29] in that motile and matrix sites contribute differently to mechanical resistance, resulting in motile sites being shoved around more during biofilm development. Thus, while the shoving capacity should be viewed as a general way to limit cell growth to a leading region of the biofilm, which is a ubiquitously observed property of biofilm growth, it also incorporates the appropriate mechanical properties of matrix and motile cells, allowing us to investigate the purely mechanical mechanisms of pattern formation. We note that the shoving capacity is best interpreted in this purely mechanical sense, as any interpretation of it as resulting from nutrient limitation would require more complex modifications to our model.

Finally, if at any step of the simulation there is a motile site at the edge of the biofilm, it "disperses" and is removed from the colony, which is a reasonable assumption based on a previous observation of passive escape of motile cells from the edges of biofilms [36].

Simulating biofilm growth from a small group of initial sites, our model produces colonies with a distinctive motile-matrix pattern. Matrix sites surround a fractal-like motile interior. Figure 2(g) shows the output of the model for $C_{\mathrm{sh}} = 12$, $\langle\alpha\rangle = 1$, $\langle\beta\rangle = 2$, and $\sigma_\alpha = \sigma_\beta = 0.1$. In our simulations, the interior pattern of motile sites eventually becomes frozen in place after the width of exterior matrix sites exceeds the shoving capacity [Fig. 4(c) and Supplemental Material Fig. S1 [37]].

In principle, our model requires choosing (1) the initial arrangement of cell phenotypes, (2) the mean growth time, (3) the standard deviation in growth time, (4) the mean motile cell biomass $\langle\alpha\rangle$, (5) the mean matrix cell biomass $\langle\beta\rangle$, (6) the standard deviations in these biomasses σ_α and σ_β, and (7) the shoving capacity C_{sh}. However, as mentioned above, the simulation time is rescaled by the mean growth time, and the standard deviation in growth time is set to the observed value of 10%; this removes choices (2) and (3). Changes in the absolute magnitudes of $\langle\alpha\rangle$ and $\langle\beta\rangle$ simply rescale the relevant range for C_{sh}, making only their ratio important; this combines choices (4) and (5). The biomass standard deviations do not matter if they are sufficiently small, which is reasonable given the strong phenotypic differences between motile and matrix cells; this removes choice (6). Therefore, we are left with the initial arrangement and two key parameters: $\langle\beta\rangle/\langle\alpha\rangle$ and C_{sh}. We wanted to know how the initial arrangement of phenotypes, as well as the values of the key model parameters, influenced the predicted motile-matrix patterns.

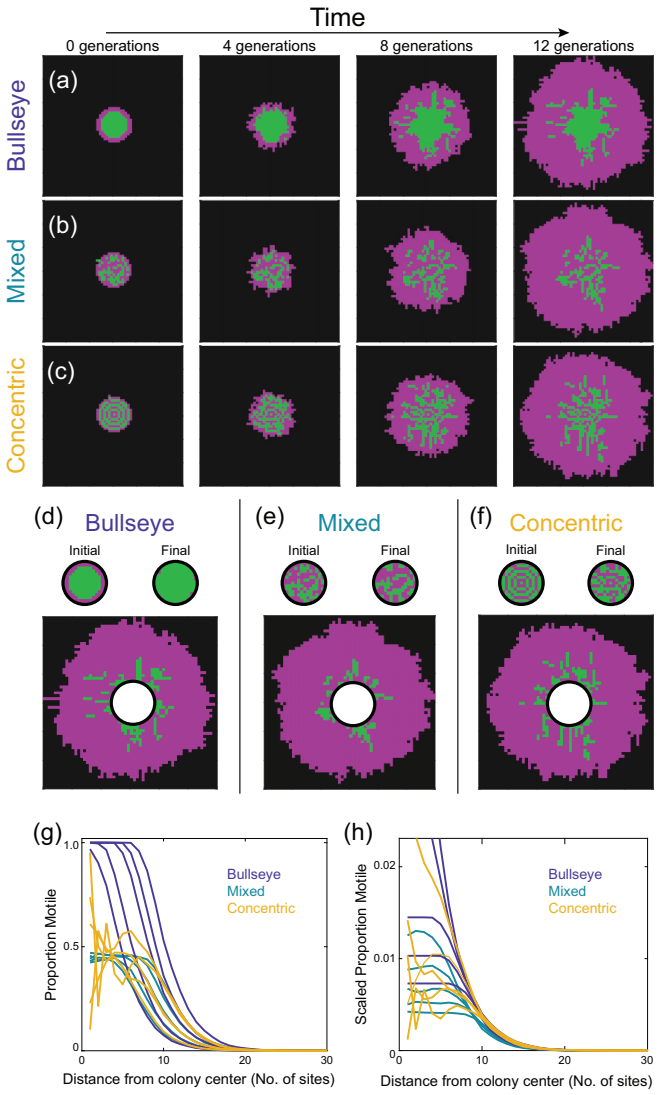


FIG. 3. Dependence of patterns on initial conditions. The evolution of the system from three different initial conditions: (a) bullseye, (b) mixed, and (c) concentric. (d)–(f) Visual isolation of the region of the biofilm unaffected by the initial condition. (g) Proportion of motile sites within a ring at a particular distance from the center of the final pattern, as a function of the distance. Each line within an initial condition subset represents a different initial radius value ranging from $R_0 = 4$ to $R_0 = 8$ (larger initial radii correspond to falloffs farther from the center). (h) When the proportion of motile sites is divided by the initial number of motile sites, a collapse is observed beyond a distance from the center corresponding to the initial condition. Parameter values are $C_{\mathrm{sh}} = 12$, $\langle\alpha\rangle = 1$, $\langle\beta\rangle = 2$, and $\sigma_\alpha = \sigma_\beta = 0.1$.

C. Dependence of phenotypic patterns on initial conditions

To investigate how our model's predictions depend on the initial phenotypic arrangement, we carried out simulations with three different initial conditions (Fig. 3). In the first case, termed "bullseye," a layer of matrix sites surrounded a group of motile sities in the initial inoculum [Fig. 3(a)]. In the second condition, "mixed," the initial colony consisted of a mixture of motile and matrix phenotypes, with each initially occupied lattice site having equal probability of being either type [Fig. 3(b)]. The third condition, "concentric," consisted of alternating rings of each type with matrix sites residing on the outermost ring. We show examples of our model's simulated biofilm growth from these three conditions in Figs. 3(a), 3(b), and 3(c).

Each starting condition appeared to create a different final pattern [Figs. 3(a), 3(b), and 3(c), right]. However, we observed that, in the final state for each condition, the

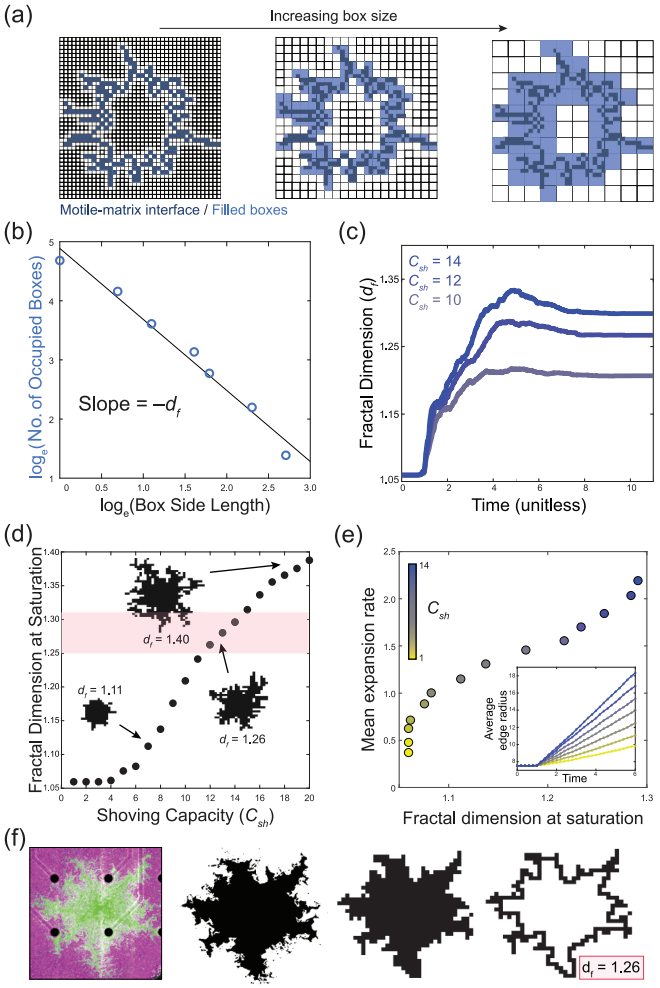


FIG. 4. Fractal dimension of the phenotype interface. Fractal dimension is found using the box-counting method: (a) Grids of different box sizes are fit to the internal motile subpopulation to produce a graph like (b). The negative of the slope is the fractal dimension. (c) Fractal dimension over time for three different C_{sh} values shows that d_f increases to a point of saturation. (d) The fractal dimension at saturation increases with the shoving capacity. Parameter values are $\langle\alpha\rangle = 1$, $\langle\beta\rangle = 2$, and $\sigma_\alpha = \sigma_\beta = 0.1$. Black images give examples of simulated motile clusters of various fractal dimensions. The pink band indicates the range of experimental fractal dimensions. Note that the x axis (C_{sh}) can be interpreted as the dimensionless scaled quantity C_{sh}/α and because $\alpha = 1$, $C_{\mathrm{sh}}/\alpha = C_{\mathrm{sh}}$. (e) Saturating d_f vs mean colony expansion rate (computed from inset radius vs time) shows that colony growth correlates with d_f. (f) Fractal dimension analysis of experimental biofilms. Experimental images segmented according to $\mathrm{P_{hag}}$-YFP intensity, down-sampled to the same resolution as simulations, and fractal dimension is computed with box counting. The fractal dimension is $d_f = 1.26 \pm 0.03$ ($N = 4$).

regions of the colonies that were populated only by the model's simulated growth, and not by the initial inoculum, exhibited qualitatively similar patterns: motile branches penetrated into an outer layer of matrix producers. We highlight this in Figs. 3(d), 3(e), and 3(f). When the initial group of sites is visually excluded, the ability to distinguish which final pattern results from each distinct initial condition is lost.

We next sought to quantify the final motile-matrix patterns generated from each initial condition. We observed that every pattern simulated by our model featured motile sites in the interior surrounded by matrix sites. To quantify these patterns, we computed, for a given ring of sites, the motile proportion as a function of the distance of the ring from the colony center. In Fig. 3(g), we plot such curves for bullseye, mixed, and concentric conditions. Each curve is an average of 300 simulations run under the same conditions (see example replicates in Fig. S2 [37]). Within each initial condition, we analyzed three different initial colony radii. The initial proportion of motile sites was kept roughly constant for each initial condition when the inoculation radius changed (with slightly more variation in the concentric condition than in mixed or bullseye). All cases featured patterns where the fraction of motile sites is high in the center and decays near the edge. However, the curves differed in key ways. For different initial conditions, the motile fraction dropped off at different distances from the colony center. The same was true for the case of different initial radii within the same initial condition subset: larger initial colonies exhibited a larger radius at which the motile proportion dropped off [Fig. 3(g)].

Motivated by our observation in Figs. 3(d)–3(f) that biofilm regions that were populated only by model growth looked the same, we thought that perhaps the curves of Fig. 3(g) would collapse if the initial conditions were taken into account in the proper way. When we scaled the proportion of motile sites throughout different radii by the initial number of motile sites, we produced the curves in Fig. 3(h). In this case, we observed a collapse not only of all curves within an initial condition subset, but also of curves representing all initial conditions. The point of collapse on the x axis of Fig. 3(h) represents the radius below which the initial condition has an effect. This radius increases with the value of C_{sh} (See Supplemental Material Fig. S1 for varying C_{sh} [37]), because at larger C_{sh}, interior cells are able to shove for a longer period of growth. Beyond the point in Fig. 3(h), all scaled curves collapse, illustrating that our model simulates the motile distribution within biofilms during growth in a way that is insensitive to the initial arrangement. This result suggested that the growth dynamics of our model produce patterns of motile and matrix cells that are robust to changes in the initial cell arrangement.

D. Fractal interface formation between phenotypes

In simulated biofilms, the motile-matrix interface appeared to have a fractal character [Figs. 2(g) and 3] qualitatively similar to those in experiments (Fig. 1). Fractal interfaces have been observed in a variety of microbial systems, including the outer edge of bacterial colonies [38] and the trajectories of motile bacteria [39]. We chose to quantify the patterns predicted by our model with fractal dimension [Figs. 4(a) and 4(b)]. At each time point for model biofilms, we found the outline of the motile-matrix interface and computed its fractal dimension using box counting [40]. In this method, the number of pixels containing a part of the interface is counted. Space is then divided into larger and larger boxes and, for each box size, the number of occupied boxes is counted [Fig. 4(a)]. The number of occupied boxes scales with some power of

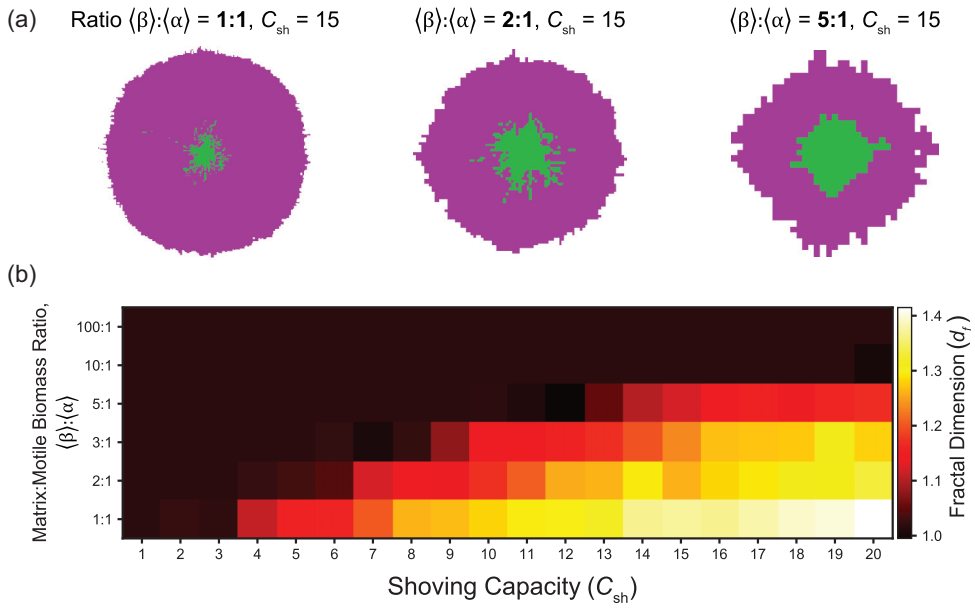


FIG. 5. Dependence of fractal interface on motile-matrix biomass ratio. (a) Examples of simulated biofilms with the same C_{sh}, but different ratios of motile-to-matrix biomass, $\langle\beta\rangle : \langle\alpha\rangle$. Note that the three examples are depicted at different scales. (b) A heatmap showing fractal dimension for a range of values of C_{sh} and biomass ratio $\langle\beta\rangle : \langle\alpha\rangle$. Parameter values are $\sigma_\alpha = \sigma_\beta = 0.1$. Note that the x axis (C_{sh}) can be interpreted as the dimensionless scaled quantity C_{sh}/α and because $\alpha = 1$ in all simulations, $C_{sh}/\alpha = C_{sh}$.

the box size depending on the shape of the interface. That exponent is the fractal dimension. It is 1 for a simple line, 2 for a two-dimensional plane, and between 1 and 2 for a rough interface like that in our model. To extract the fractal dimension for the interface in our model, we fitted a regression line to a log-log plot of box size vs occupied boxes. The negative slope of the regression line is the fractal dimension, d_f [Fig. 4(b)].

For simulated biofilms initialized with a bullseye pattern, the fractal dimension started out near 1 because the motile-matrix interface was smooth for this condition. Once simulated growth commenced, sites shoved each other out of the way as they grew, roughening the interface, and increasing the fractal dimension. However, once the outer matrix layer thickness exceeded the shoving capacity, C_{sh}, the motile-matrix interface froze into place and the fractal dimension saturated [Fig. 4(c)]. Saturation occurs after fractal dimension reaches a peak and declines due to shoving separating small motile clusters from the inner motile population (Fig. S3) [37]. Because increasing the shoving capacity increases the time during which sites can grow and push each other around, we hypothesized that the saturating fractal dimension would increase with shoving capacity. After simulating biofilm growth for a range of shoving capacities, we found that saturating fractal dimension does indeed increase with shoving capacity [Fig. 4(d)]. The behavior of the fractal dimension in Fig. 4(c) is robust to changes in site growth decisions; for example, whether the direction of growth is random or preferential to the previous growth direction chosen by the parent site (Fig. S4) [37]. By computing the radius over time for biofilms with a range of shoving capacities, we also found that biofilms with higher fractal dimensions also expanded faster on average [Fig. 4(e)]. We wanted to know what the fractal dimension of the motile-matrix interface in our experimental images was. To determine the experimental fractal dimension, we thresholded biofilm images, found the outline of the interior motile population, and performed box counting. To account for the fact that a lattice site corresponds to a coarse-grained packet of cells, we down-sampled our experimental images to make them the same resolution as the model [Fig. 4(f)]. We found that the experimental fractal dimension was 1.26 ± 0.03 ($N = 4$), which is within the possible range predicted by the model [Fig. 4(d)].

E. Dependence of fractal dimension on motile and matrix biomass difference

We hypothesized that the phenotypic interface in our model would depend on the difference in biomass between motile and matrix sites. To determine how mechanical differences between motile and matrix changed the model's predicted interface, we simulated colonies with a range of matrix-to-motile average biomass ratios, $\rho_{\beta\alpha} = \langle\beta\rangle : \langle\alpha\rangle$. We found that the interface between phenotypes became smoother as the matrix-motile biomass ratio increased [Fig. 5(a)]. This makes sense because at very high matrix-motile ratios, interior motile sites can barely push matrix sites at all and the interface remains smooth. In contrast, when both phenotypes have the same biomass ($\rho_{\beta\alpha} \approx 1:1$), motile sites can easily push matrix, resulting in a rough interface. To quantify this effect, we computed the interface fractal dimension for a range of $\rho_{\beta\alpha}$ values. Specifically, we simulated $\{\langle\alpha\rangle, \langle\beta\rangle\} = [\{1, 1\}, \{1, 2\}, \{1, 3\}, \{1, 5\}, \{1, 10\}, \{1, 100\}]$ with shoving capacities from $C_{sh} = 1$ to $C_{sh} = 20$. The resulting fractal dimensions are plotted in the heatmap of Fig. 5(b). We found that as the matrix-motile biomass ratio increased, the limiting fractal dimension decreased and, above a certain ratio, the interface would not roughen at all. This maximum ratio at

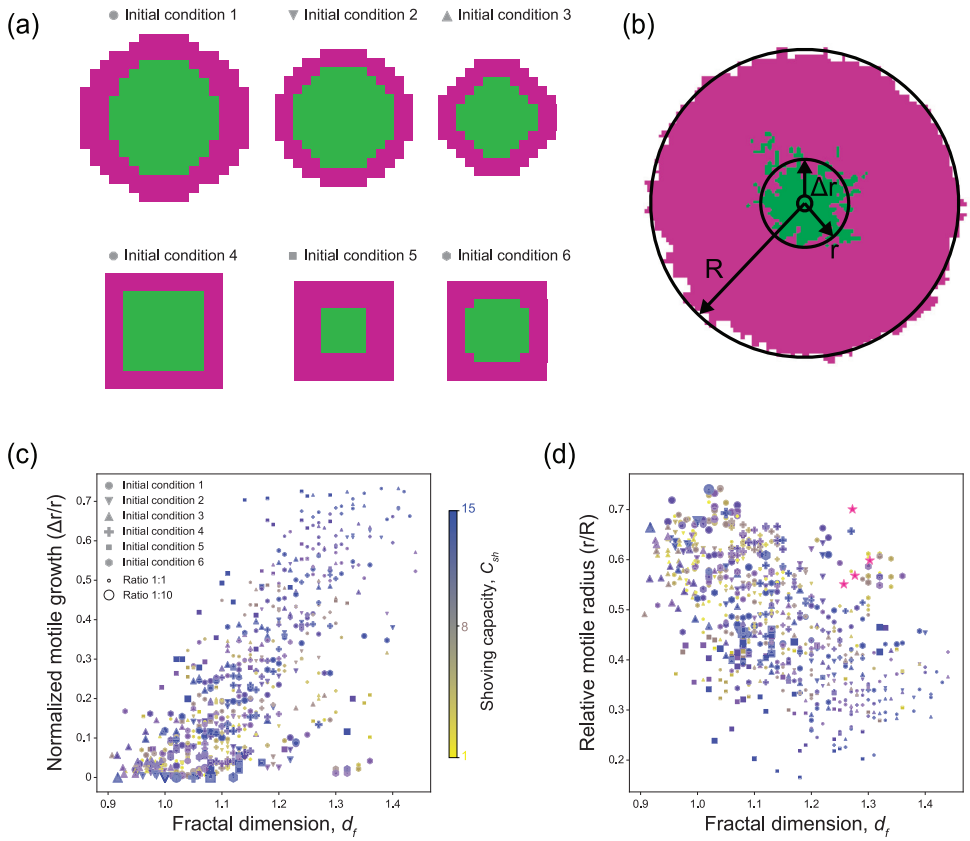


FIG. 6. Relationship between fractal interface and biofilm composition. (a) Several different initial conditions simulated for a range of C_{sh} and biomass ratio values. (b) Schematic shows three parameters of motile and matrix radial expansion. (c) Scatterplot of scaled motile growth ($\frac{\Delta r}{r}$) vs fractal dimension. Marker shape indicates initial arrangement, marker size indicates motile-matrix biomass ratio (smallest 1:1, largest 1:10), and marker color indicates shoving capacity. Pearson's correlation is $r = 0.70$. For each unique set of parameters and initial conditions, five simulations were performed, each of which is included in the scatterplot. In instances where the fractal dimension is less than 1, we have verified that the fitted slope from the box-counting method includes the value 1 within its uncertainty window. (d) Scatterplot of the same data for scaled motile radius ($\frac{r}{R}$) vs fractal dimension. Pearson's correlation is $r = -0.65$. Parameter values are $\sigma_\alpha = \sigma_\beta = 0.1$. Pink stars represent experimental data.

which roughening occurs depended on the shoving capacity C_{sh} [Fig. 5(b)]. Thus, depending on $\rho_{\beta\alpha}$ and C_{sh}, the model predicted biofilms that either retained smooth interfaces [dark region of Fig. 5(b)] or roughened the interface [bright region of Fig. 5(b)]. As such, we attain a mechanistic understanding of the conditions that give rise to a fractal-like interface: a small matrix-to-motile biomass ratio and a large shoving capacity.

Our test of parameter dependence (Fig. 5) suggested that the model could predict a wide range of fractal interfaces by simply changing C_{sh} and $\rho_{\alpha\beta}$. However, we noticed that in simulated biofilms with low fractal dimensions (i.e., smooth interfaces), the fractal dimension froze after relatively little growth [Fig. 5(a), right]. We therefore wondered whether there was a relationship between inner motile growth and the interface fractal dimension. To investigate this relationship, we simulated biofilms with a variety of C_{sh} values, $\rho_{\alpha\beta}$ ratios, and initial site configurations. We chose initial inoculum conditions that had a range of radii and proportions of each phenotype [Fig. 6(a)]. For each simulated biofilm, we extracted the fractal dimension, as well as the average radial expansion of both the inner motile population and the entire biofilm from the start of the simulation to the time when the interface froze [Fig. 6(b)]. After examining fractal dimension and growth for a wide range of model parameters, we found two correlations: (1) the radial expansion of the motile population relative to its initial radius [$\Delta r/r$, Fig. 6(b)] correlated positively with fractal dimension [Fig. 6(c)] and (2) the ratio of motile radius to total biofilm radius [r/R, Fig. 6(b)] correlated negatively with fractal dimension [Fig. 6(d)]. The first correlation arises from the observation that larger $\Delta r/r$ signifies more motile growth from the initial inoculum. More growth generally means longer fractal motile branches. For the second correlation, a smaller r/R ratio is indicative of a larger gap between the internal motile population and the surrounding matrix population, again evidence for longer fractal branches. In contrast, a phenotypic interface closer to the edge of the biofilm results in a larger r/R, meaning the motile pattern freezes earlier. In general both correlations fit into the same explanation that if the motile sites at the interface upon initialization have an opportunity to grow, growth events are more likely to occur in these regions as there are fewer accumulated matrix sites and therefore less biomass to push. The result is motile sites forming branches where longer branches fall into the regime of high $\Delta r/r$ and low r/R where we observe the largest fractal dimensions.

To further compare the experimental properties with the model output, we sought to compute the average radii of the interface and of the biofilm when the pattern freezes, i.e., r and R of Fig. 6. Because the fluorescent reporters of our experimental strain did not exhibit enough initial fluorescence for segmentation, we could not experimentally measure Δr. However, we were able to estimate the ratio r/R for the $N = 4$ biofilms observed, and the results are shown in Fig. 6(d) (pink stars). We found that the experimental values were close together and generally fell within the range of model outputs, tending toward the upper right of the $(d_f, r/R)$ plot. When comparing the experimental values to model output in the Fig. 6(d) scatterplot, we observed that a range of C_{sh} values reproduce similar d_f values (colors of model symbols) to the experimental data, but that model output with similar $\frac{r}{R}$ and C_{sh} to experiments had $\rho_{\beta\alpha} \approx 3:1 - 5:1$. The initial condition had little effect. These observations constrain our model's parameter values in order to produce similar patterns to those observed in our experimental system.

These experimental results do not demonstrate that the mechanical mechanisms of our model drive phenotypic pattern formation in *B. subtilis*, but they show that our model predictions are quantitatively consistent with the properties of experimental biofilms.

These correlations illustrate general constraints on growth and pattern formation predicted by the model. Specifically, across a broad spectrum of parameters and initial conditions, biofilms that generate fractal interfaces will also exhibit more motile expansion, but that motile population will constitute a smaller percentage of the colony once the pattern is formed. Our model predicts a relationship between the mechanical properties of phenotypes and the phenotypic content of biofilms.

III. MATERIALS AND METHODS

A. Model

The Code for the model has been posted to the GitHub repository [41].

Determining the fractal dimension of model output

The fractal dimension is found using the box-counting method. Within the model, first the internal shape is recognized through a recursive shape fill method. From this, the perimeter of this shape is isolated and the box-counting method enforced. In order to correctly identify the dimension of the shape, the grids of different box sizes are fit to the perimeter identified. That is, as the biofilm grows, the dimensions of the grids used in this analysis will change as well. At each time step, we produce a graph of ln(box size) vs ln(occupied boxes). The negative slope of a regression line is taken as the fractal dimension of the internal motile subpopulation. The number of points within this plot is reflective of the number of grids of different box sizes fit to the perimeter. The algorithm attempts to maximize the number of points while limiting the overall dimension of the grid used to cover the internal shape. When repeated over numerous time steps as the biofilm grows and then averaging over hundreds of systems, we are able to produce the results shown in Fig. 4.

B. Experiment

We grew biofilms in a microfluidic device as described in [31]. Biofilm growth media consisted of liquid MSgg medium containing 5 mM potassium phosphate buffer (pH 7.0), 100 mM MOPS buffer (pH 7.0, adjusted using NaOH), 2 mM $MgCl_2$, 700 μm $CaCl_2$, 5 μm $MnCl_2$, 100 μm $FeCl_3$, 1 μm $ZnCl_2$, 2 μm thiamine HCl, 0.1 mM sodium citrate, 0.5% (v/v) glycerol, and 0.4% (w/v) monosodium glutamate. Media were made from stock solutions immediately before experiments, and the stock solution of glutamate was made fresh daily. We acquired images with a Fluoview FV3000 scanning confocal microscope (Olympus Corp.) using a 10×, 0.3 NA air objective. We performed experiments with a modified *B. subtilis* NCIB3610 strain with Venus yellow fluorescent protein (YFP) fused to the *hag* promoter and mCherry fused to the *tapA* promoter.

C. Data analysis

We analyzed images in Fiji [42]. In order to accurately compare our model to our experimental data, we first needed to coarse-grain the experimental images, ensuring that the experimental pixel size was comparable to the cell size of our model. To achieve accurate scaling, we first cropped the time-lapse tiff stack for the YFP channel so the saturated fractal filled the entire frame. At this point, select frames were analyzed individually and were only chosen after a clear bimodal distribution arose in the YFP channel—the brighter peak representing the high concentration of motile cells inside the motile-matrix interface and the dimmer peak representing regions of the biofilm containing mostly matrix cells. This step ensured that there was minimal bias in thresholding, as images were thresholded simply by selecting the brighter peak of inner motile cells. After filling the holes of the thresholded image, we could resize the entire frame to 40 by 40 pixels, so it was comparable to the size of the saturated fractal in the computer model. Next, we converted the threshold to binary and the fractal was cropped to fit the entire frame; this ensures a more accurate measure of its fractal dimension. We could finally outline the interface and use Fiji's fractal box count tool, selecting the same sized boxes used for the computer model's fractal analysis, to identify the fractal dimension of the experimental interface.

IV. DISCUSSION

We have presented a simple, agent-based model that accounts for multiple features of patterns formed by motile and matrix cell phenotypes in *B. subtilis* colonies. Specifically, the model addresses two key questions: (1) how do motile-matrix patterns depend on initial conditions? (2) How do mechanical interactions between heterogeneous phenotypes contribute to patterning? On the first question, we found that in uncolonized regions of space, our mechanical growth model's dynamics create motile patterns that are robust to the initial arrangement. This arises from the model spatially distributing phenotypes not only through growth and inheritance, but also by mechanical shoving during replication. For three different starting arrangements, we found that the limiting pattern depended strongly on the initial condition within the initial

inoculum radius, but beyond that radius the scaled density of motile sites collapsed for all three initial patterns. On the second question, the model predicted that varying the mechanical properties of growth can dramatically alter phenotypic patterns, but that growth and patterning are statistically constrained: biofilms that produce fractal interfaces exhibit more motile growth. It is not clear what, if anything, is the benefit of creating a fractal interface between cells of different phenotypes. Two possibilities are that creating a fractal interface expands biofilms faster due to excessive cell shoving [Fig. 4(e)] or that a fractal interface minimizes the distance between different cell types (Fig. S5 [37]) to make diffusible resource sharing more efficient.

Our model greatly simplifies *B. subtilis* colony growth. The model does not take into account multiple factors that could influence phenotypic patterning; for example, nutrient availability [43], phenotypic switching [21], cell shape [26], or the fact that cells grow continuously [30] and not in discrete time. However, despite these simplifications, it makes predictions that are consistent with experimental data and demonstrates a potential mechanical mechanism for spatial distributions of phenotypes within biofilms. Furthermore, our model establishes a starting point for more detailed agent-based simulations that take into account other factors such as active cell movement, metabolism, or cell shape. For example, by incorporating nutrient-dependent growth and pressure from cell pushing, our model could potentially be extended to disentangle the mechanical and nutrient-based effects limiting biofilm expansion. Our model could also probe the dynamics of pattern formation in bacterial biofilms by, for example, comparing the time between initial conditions and the phenotypic pattern "freezing" [Fig. 4(c)]. In our model, the pattern often freezes after fewer than ten generation times, whereas experimentally it freezes after 20–30 cell division times. These comparisons, however, are not straightforward due to the coarse-graining of the model: the model's generation time is for a group of cells to push, whereas the experimental doubling time is for individual cells to divide. To make these comparisons would require more investigation into the relationship between cell division time and physical biofilm expansion.

Our finding that the final pattern only depends on the initial conditions at low radii, and beyond this the resulting pattern is mechanistically determined, is something that we could not have found from experiments. The reason is that there is significant uncertainty in our ability to determine the differentiation state at early time points. This is one advantage to mechanistic modeling: it allows one to validate experiments in particular regimes, and in doing so, makes predictions for regimes not yet accessible.

Attempts to use agent-based or statistical physics models for living systems must take into account an essential feature of cells and organisms: they not only sense their environment, they also change it. This feedback can lead to remarkable phenomena that collectives of cells can take advantage of. Our results capture this phenomenon in a simple way. As biofilm cells grow, they create a constrained environment, altering patterns of growth and leading to a wide variety of potential cell-type patterns.

ACKNOWLEDGMENTS

We acknowledge Neil Marya, Patrick Powers, and members of the Larkin Lab for comments on the paper. This work was supported by a pilot grant from the NSF-Simons Center for Quantitative Biology, Award No. 1764421 (J.W.L. and A.M.), the Burroughs Wellcome Fund (Career Award at the Scientific Interface, J.W.L.), the National Science Foundation (Grant No. 2027108, J.W.L.; Grant No. 1852266, C.B.; Grant No. PHY-2118561, A.M.), the National Institute of General Medical Sciences (Grant No. R35GM142584, J.W.L.; Grants No. R01GM121888 and No. R35GM139645, G.M.S.), the Simons Foundation (Award No. 376198, A.M.), the Defense Advanced Research Projects Agency (Grant No. HR0011-16-2-0035, G.M.S.), and the Howard Hughes Medical Institute (Simons Foundation Faculty Scholar Award, G.M.S.).

The authors declare no conflict of interest.

DATA AVAILABILITY

The data that support the findings of this article are openly available [41].

[1] J.-W. Veening, W. K. Smits, and O. P. Kuipers, Bistability, epigenetics, and bet-hedging in bacteria, Annu. Rev. Microbiol. **62**, 193 (2008).

[2] N. Nikolic, F. Schreiber, A. Dal Co, D. J. Kiviet, T. Bergmiller, S. Littmann, Marcel M. M. Kuypers, and M. Ackermann, Cell-to-cell variation and specialization in sugar metabolism in clonal bacterial populations, PLoS Genet. **13**, e1007122 (2017).

[3] H. Maamar, A. Raj, and D. Dubnau, Noise in gene expression determines cell fate in *Bacillus subtilis*, Science **317**, 526 (2007).

[4] D. Lopez, H. Vlamakis, and R. Kolter, Generation of multiple cell types in *Bacillus subtilis*, FEMS Microbiol. Rev. **33**, 152 (2009).

[5] H. Vlamakis, Y. Chai, P. Beauregard, R. Losick, and R. Kolter, Sticking together: Building a biofilm the *Bacillus subtilis* way, Nat. Rev. Microbiol. **11**, 157 (2013).

[6] D. B. Kearns and R. Losick, Cell population heterogeneity during growth of *Bacillus subtilis*, Genes Dev. **19**, 3083 (2005).

[7] C. R. Armbruster, C. K. Lee, J. Parker-Gilham, J. de Anda, A. Xia, K. Zhao, K. Murakami, B. S. Tseng, L. R. Hoffman, F. Jin, C. S. Harwood, G. C. Wong, and M. R. Parsek, Heterogeneity in surface sensing suggests a division of labor in *Pseudomonas Aeruginosa* populations, eLife **8**, e45084 (2021).

[8] N. Steinberg, A. Keren-Paz, Q. Hou, S. Doron, K. Yanuka-Golub, T. Olender, R. Hadar, G. Rosenberg, R. Jain, J. Cámara-Almirón, D. Romero, S. van Teeffelen, and I. Kolodkin-Gal, The extracellular matrix protein tasa is a developmental cue that maintains a motile subpopulation within *Bacillus subtilis* biofilms, Sci. Signal. **13**, eaaw8905 (2020).

[9] P. S. Stewart and M. J. Franklin, Physiological heterogeneity in biofilms, Nat. Rev. Microbiol. **6**, 199 (2008).

[10] H. Vlamakis, C. Aguilar, R. Losick, and R. Kolter, Control of cell fate by the formation of an architecturally complex bacterial community, Genes Dev. **22**, 945 (2008).
[11] G. O'Toole, H. B. Kaplan, and R. Kolter, Biofilm formation as microbial development, Annu. Rev. Microbiol. **54**, 49 (2000).
[12] P. Stoodley, K. Sauer, D. G. Davies, and J. W. Costerton, Biofilms as complex differentiated communities, Annu. Rev. Microbiol. **56**, 187 (2002).
[13] S. M. Rosenberg, Life, death, differentiation, and the multicellularity of bacteria, PLoS Genet. **5**, e1000418 (2009).
[14] H.-C. Flemming and J. Wingender, The biofilm matrix, Nat. Rev. Microbiol. **8**, 623 (2010).
[15] D. B. Kearns, F. Chu, S. S. Branda, R. Kolter, and R. Losick, A master regulator for biofilm formation by *Bacillus subtilis*, Mol. Microbiol. **55**, 739 (2005).
[16] K. P. Lemon, A. M. Earl, H. C. Vlamakis, C. Aguilar, and R. Kolter, Biofilm development with an emphasis on *Bacillus subtilis*, in *Bacterial Biofilms*, Current Topics in Microbiology and Immunology, Vol. 322, edited by T. Romeo (Springer Berlin Heidelberg, Berlin, Heidelberg, 2008), pp. 1–16.
[17] A. D. Grossman, Genetic networks controlling the initiation of sporulation and the development of genetic competence in *Bacillus subtilis*, Annu. Rev. Genet. **29**, 477 (1995).
[18] S. Arnaouteli, N. C. Bamford, N. R. Stanley-Wall, and Á. T. Kovács, *Bacillus subtilis* biofilm formation and social interactions, Nat. Rev. Microbiol. **19**, 600 (2021).
[19] S. Srinivasan, I. D. Vladescu, S. A. Koehler, X. Wang, M. Mani, and S. M. Rubinstein, Matrix production and sporulation in *Bacillus subtilis* biofilms localize to propagating wave fronts, Biophys. J. **114**, 1490 (2018).
[20] Y. Chai, F. Chu, R. Kolter, and R. Losick, Bistability and biofilm formation in *Bacillus subtilis*, Mol. Microbiol. **67**, 254 (2008).
[21] T. M. Norman, N. D. Lord, J. Paulsson, and R. Losick, Memory and modularity in cell-fate decision making, Nature (London) **503**, 481 (2013).
[22] M. Asally, M. Kittisopikul, P. Rué, Y. Du, Z. Hu, T. Çağatay, A. B. Robinson, H. Lu, J. Garcia-Ojalvo, and G. M. Süel, Localized cell death focuses mechanical forces during 3d patterning in a biofilm, Proc. Natl. Acad. Sci. USA **109**, 18891 (2012).
[23] Y. Chai, T. Norman, R. Kolter, and R. Losick, An epigenetic switch governing daughter cell separation in *Bacillus subtilis*, Genes Dev. **24**, 754 (2010).
[24] A. Persat, C. D. Nadell, M. K. Kim, F. Ingremeau, A. Siryaporn, K. Drescher, N. S. Wingreen, B. L. Bassler, Z. Gitai, and H. A. Stone, The mechanical world of bacteria, Cell **161**, 988 (2015).
[25] D. Volfson, S. Cookson, J. Hasty, and L. S. Tsimring, Biomechanical ordering of dense cell populations, Proc. Natl. Acad. Sci. USA **105**, 15346 (2008).
[26] W. P. J. Smith, Y. Davit, J. M. Osborne, W. Kim, K. R. Foster, and J. M. Pitt-Francis, Cell morphology drives spatial patterning in microbial communities, Proc. Natl. Acad. Sci. USA **114**, E280 (2017).
[27] T. J. Rudge, F. Federici, P. J. Steiner, A. Kan, and J. Haseloff, Cell polarity-driven instability generates self-organized, fractal patterning of cell layers, ACS Synth. Biol. **2**, 705 (2013).
[28] J. J. Winkle, O. A. Igoshin, M. R. Bennett, K. Josić, and W. Ott, Modeling mechanical interactions in growing populations of rod-shaped bacteria, Phys. Biol. **14**, 055001 (2017).
[29] A. V. Narla, D. B. Borenstein, and N. S. Wingreen, A biophysical limit for quorum sensing in biofilms, Proc. Natl. Acad. Sci. USA **118**, e2022818118 (2021).
[30] A. Martínez-Calvo, C. Trenado-Yuste, H. Lee, J. Gore, N. S. Wingreen, and S. S. Datta, Interfacial morphodynamics of proliferating microbial communities, Phys. Rev. X **15**, 011016 (2025).
[31] C. J. Comerci, A. L. Gillman, L. Galera-Laporta, E. Gutierrez, A. Groisman, J. W. Larkin, J. Garcia-Ojalvo, and G. M. Süel, Localized electrical stimulation triggers cell-type-specific proliferation in biofilms, Cell Syst. **13**, 488 (2022).
[32] C. Picioreanu, J.-U. Kreft, and M. C. M. van Loosdrecht, Particle-based multidimensional multispecies biofilm model, Appl. Environ. Microbiol. **70**, 3024 (2004).
[33] K. Drescher, J. Dunkel, C. D. Nadell, S. van Teeffelen, I. Grnja, N. S. Wingreen, H. A. Stone, and B. L. Bassler, Architectural transitions in *Vibrio cholerae* biofilms at single-cell resolution, Proc. Natl. Acad. Sci. USA **113**, E2066 (2016).
[34] B. J. Cooley, T. W. Thatcher, S. M. Hashmi, G. L'her, H. H. Le, D. A. Hurwitz, D. Provenzano, A. Touhami, and V. D. Gordon, The extracellular polysaccharide Pel makes the attachment of *P. Aeruginosa* to surfaces symmetric and short-ranged, Soft Matter **9**, 3871 (2013).
[35] S. S. Branda, F. Chu, D. B. Kearns, R. Losick, and R. Kolter, A major protein component of the *Bacillus subtilis* biofilm matrix, Mol. Microbiol. **59**, 1229 (2006).
[36] P. Stoodley, S. Wilson, Luanne Hall-Stoodley, J. D. Boyle, H. M. Lappin-Scott, and J. W. Costerton, Growth and detachment of cell clusters from mature mixed-species biofilms, Appl. Environ. Microbiol. **67**, 5608 (2001).
[37] See Supplemental Material at http://link.aps.org/supplemental/10.1103/2zm9-r3qs for collapse radii at varied shoving capacity, replicates of radial motile distributions, decrease in fractal dimension as islands break off the motile interior, effect of preferred growth direction, and average distance between cells of different phenotypes.
[38] T. Vicsek, M. Cserző, and V. K. Horváth, Self-affine growth of bacterial colonies, Phys. A (Amsterdam, Neth.) **167**, 315 (1990).
[39] H. Koorehdavoudi, G. W. Paul Bogdan, R. Marculescu, J. Zhuang, R. W. Carlsen, and M. Sitti, Multi-fractal characterization of bacterial swimming dynamics: A case study on real and simulated *Serratia marcescens*, Proc. R. Soc. A **473**, 20170154 (2017).
[40] J. J. Gagnepain and C. Roques-Carmes, Fractal approach to two-dimensional and three-dimensional surface roughness, Wear **109**, 119 (1986).
[41] Github repository (2025), https://github.com/caelan-brooks/frac-interface-model.
[42] J. Schindelin, I. Arganda-Carreras, E. Frise, V. Kaynig, M. Longair, T. Pietzsch, S. Preibisch, C. Rueden, S. Saalfeld, B. Schmid, J.-Y. Tinevez, D. J. White, V. Hartenstein, K. Eliceiri, P. Tomancak, and A. Cardona, Fiji: An open-source platform for biological-image analysis, Nat. Methods **9**, 676 (2012).
[43] W. Zhang, A. Seminara, M. Suaris, M. P. Brenner, D. A. Weitz, and T. E. Angelini, Nutrient depletion in *Bacillus subtilis* biofilms triggers matrix production, New J. Phys. **16**, 015028 (2014).